

PROCEEDINGS OF SPIE

SPIEDigitalLibrary.org/conference-proceedings-of-spie

Kernel Flow: a high channel count scalable TD-fNIRS system

Ban, Han, Barrett, Geoffrey, Borisevich, Alex, Chaturvedi, Ashutosh, Dahle, Jacob, et al.

Han Y. Ban, Geoffrey M. Barrett, Alex Borisevich, Ashutosh Chaturvedi, Jacob L. Dahle, Hamid Dehghani, Bruno DoValle, Julien Dubois, Ryan M. Field, Viswanath Gopalakrishnan, Andrew Gundran, Michael Henninger, Wilson C. Ho, Howard D. Hughes, Rong Jin, Julian Kates-Harbeck, Thanh Landy, Antonio H. Lara, Michael Leggiero, Gabriel Lerner, Zahra M. Aghajan, Michael Moon, Alejandro Ojeda, Isai Olvera, Meric Ozturk, Sangyong Park, Milin J. Patel, Katherine L. Perdue, Wing Poon, Zachary P. Sheldon, Benjamin Siepser, Sebastian Sorgenfrei, Nathan Sun, Victor Szczepanski, Mary Zhang, Zhenye Zhu, "Kernel Flow: a high channel count scalable TD-fNIRS system," Proc. SPIE 11663, Integrated Sensors for Biological and Neural Sensing, 116630B (5 March 2021); doi: 10.1117/12.2582888

SPIE.

Event: SPIE BiOS, 2021, Online Only

Kernel Flow: A high channel count scalable TD-fNIRS system

Han Y. Ban^a, Geoffrey M. Barrett^a, Alex Borisevich^a, Ashutosh Chaturvedi^a, Jacob L. Dahle^a, Hamid Dehghani^a, Bruno DoValle^a, Julien Dubois^a, Ryan M. Field^{*a}, Viswanath Gopalakrishnan^a, Andrew Gundran^a, Michael Henninger^a, Wilson C. Ho^a, Howard D. Hughes^a, Rong Jin^a, Julian Kates-Harbeck^a, Thanh Landy^a, Antonio H. Lara^a, Michael Leggiero^a, Gabriel Lerner^a, Zahra M. Aghajan^a, Michael Moon^a, Alejandro Ojeda^a, Isai Olvera^a, Meric Ozturk^a, Sangyong Park^a, Milin J. Patel^a, Katherine L. Perdue^a, Wing Poon^a, Zachary P. Sheldon^a, Benjamin Siepser^a, Sebastian Sorgenfrei^a, Nathan Sun^a, Victor Szczepanski^a, Mary Zhang^a, Zhenye Zhu^a

^aKernel, 10361 Jefferson Blvd, Culver City, CA, USA 90232

ABSTRACT

Time-Domain Near-Infrared Spectroscopy (TD-NIRS) has been considered as the gold standard of non-invasive optical brain imaging devices. However, due to the high cost, complexity, and large form-factor, it has not been as widely adopted as Continuous Wave (CW) NIRS systems. Kernel Flow is a TD-NIRS system that has been designed to break through these limitations by maintaining the performance of a research grade TD-NIRS system while integrating all of the components into a small modular device. The Kernel Flow modules are built around miniaturized laser drivers, custom integrated circuits, and specialized detectors. The modules can be assembled into a system with dense channel coverage over the entire head. We show performance similar to benchtop systems with our miniaturized device.

Keywords: fNIRS, optical brain imaging, tissue optics, time resolved spectroscopy, optical properties, imaging systems, single photon detectors, MEDPHOT

1. INTRODUCTION

Time-domain functional near-infrared spectroscopy (TD-fNIRS) systems have been considered the gold standard for optical brain imaging systems given their increased information content over continuous wave (CW) systems^{1,2}. In TD-fNIRS systems, picosecond pulses of light are emitted into tissue and arrival times of single photons are measured at nearby detectors. The distribution of photon arrival times can be parameterized to estimate tissue optical properties such as absorption (μ_a) and reduced scattering (μ_s') coefficients. The photon arrival times can also be used to localize changes in deeper tissues by analyzing the later-arriving photons (“gating”), or analyzing moments of the time-of-flight distribution³.

Despite these known advantages of TD- over CW-fNIRS data, widespread adoption of the technology has been slow due to the paucity of commercial systems⁴. The few systems that are available have few channels and slow sampling frequencies⁴. In this paper, we describe our recently developed system, Kernel Flow, which features whole-head coverage and a sampling frequency of 200 Hz for each detector. Kernel Flow was developed for scalable manufacturing which allows for inexpensive commercial production. We describe the specifications of the Kernel Flow device, benchmark it using the standard Basic Instrument Performance (BIP) and MEDPHOT protocols^{5,6}, and show example human data from a standard neuroscience task.

*Ryan.Field@kernel.com; phone 1 310 849-2870; kernel.com

2. METHODS

2.1 System Specifications

The Kernel Flow system consists of 52 modules arranged in a helmet design as shown in Figure 1. Modules are organized into 4 plates on each side of the head, covering the frontal, parietal, temporal, and occipital cortices. Each module consists of a central dual wavelength (690 nm and 850 nm) laser source surrounded by 6 hexagonally arranged detectors, each 10mm from the source. Light is transmitted from source or to detector locations using spring loaded light pipes. Source-detector separation (SDS) is 10 mm within a module, and cross module channels can also be analyzed.



Figure 1. Side view of the modules and structural plates that make up the Flow system. Each plate of modules establishes a fixed distance between the sources and detectors of the modules within the plate. The spacing between plates can be controlled using spacers that should be adjusted based on the user's head size and desired regions of interest.

Each module in the system consists of three major sub-assemblies: laser assembly, detector assembly, and the optical assembly. All 3 of these sub-assemblies are shown together in an exploded view in Figure 2. The details of each sub-assembly and the overall system architecture are presented in the following sections.

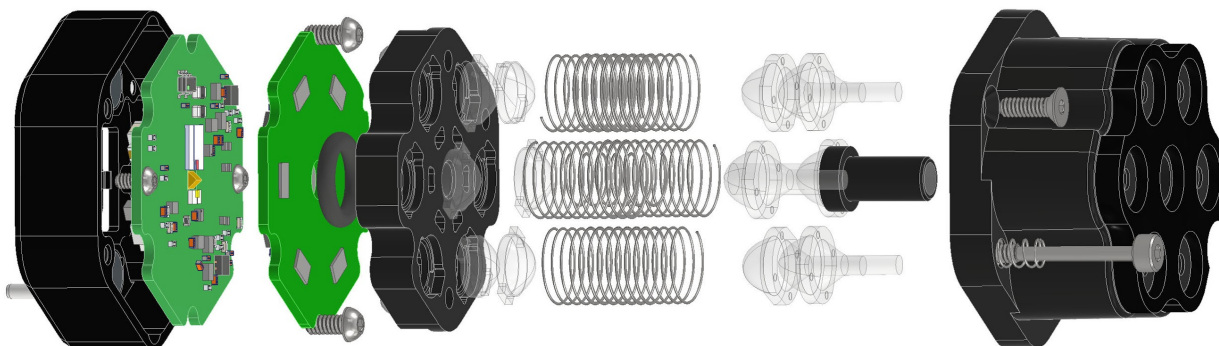


Figure 2. An exploded view showing the details of all of the module sub-assemblies.

2.1.1 System Architecture

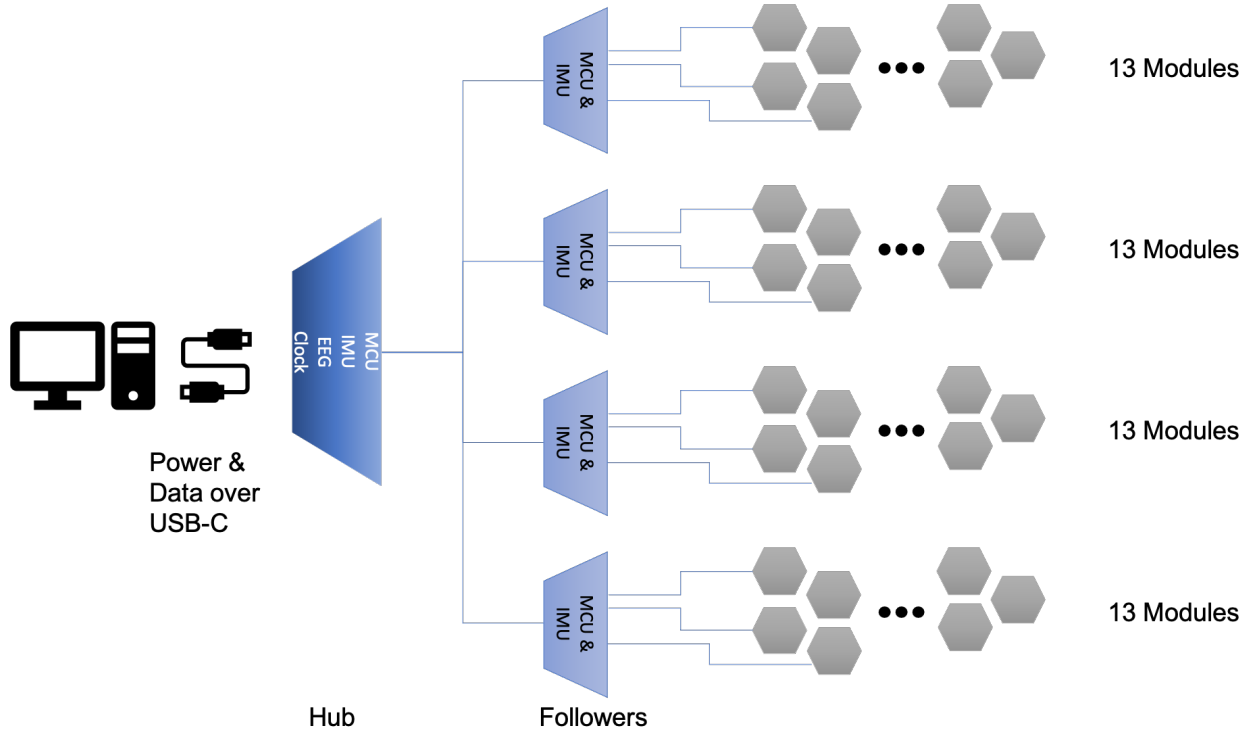


Figure 3. Overall architecture of the Flow hardware. A global clock is distributed from the primary MCU sub-assembly to all module endpoints.

The Flow system has an hierarchical architecture with electronics and wiring harnesses integrated into the helmet, as shown in Figure 3. The system is cabled over a single universal serial bus type-C (USB-C) interface that both supplies power and enables bidirectional communication between the data collection computer and the Flow system. The USB-C cable connects to the Flow system through the hub sub-assembly that includes a microcontroller unit (MCU), 9-axis inertial measurement unit (IMU), and global reference clock. In addition, the hub sub-assembly includes an 8-channel electroencephalography (EEG) amplifier and analog-to-digital converter (ADC) that is designed for connecting to active dry electrodes. The hub also handles the primary power negotiation for the Universal Serial Bus Power Delivery (USB-PD) standard and distribution of power to the rest of the system. Connected to the hub are four follower boards that serve as data aggregation points for clusters of 13 modules each. Each of these follower MCUs has additional power conditioning circuitry in addition to a 9-axis IMU.

In total the Flow system supports connection of up to 52 time-domain optical modules and includes five 9-axis IMUs, 8 EEG channels, and self-contained power management and distribution. The system works seamlessly with fewer than 52 optical modules, which enables the removal of any optical modules that are not needed for the intended experimentation. In the human studies reported in this work, we have chosen to populate two different subsets of modules, one covering the prefrontal region with 12 modules and one sampling over the somatosensory and prefrontal regions using 14 modules.

2.1.2 Laser Source Module

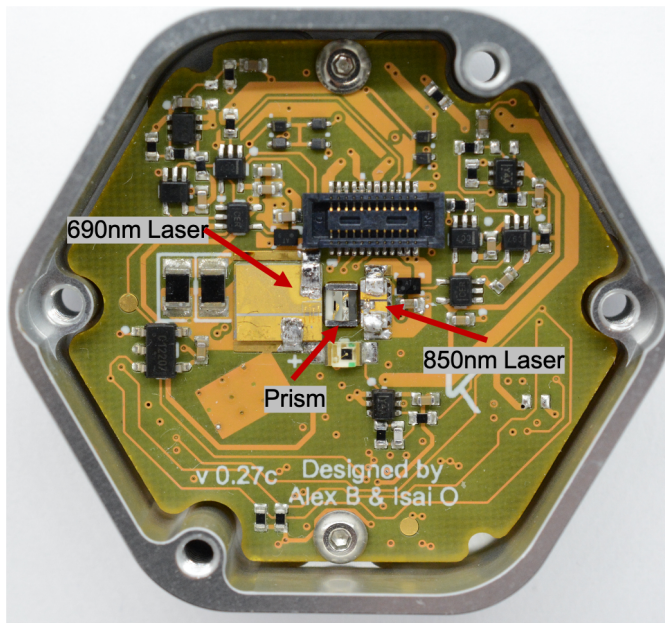


Figure 4. Laser sub-assembly showing the two different wavelengths of edge-emitting lasers, which are pulsed into a prism to combine them into the same source light pipe. The PCB assembly is secured to an aluminum base that holds the prism in place and also serves as a heat sink for the laser diodes.

The laser module sub-assembly consists of a 690 nm edge-emitting laser diode and an 850 nm edge-emitting laser diode. The two laser diodes are placed at the center of the laser sub-assembly where there is a cut-out in the printed circuit board (Figure 4). This cut-out is designed to be placed over a pedestal feature of the aluminum base where the prism is placed to redirect the edge emitting lasers in a direction perpendicular to the printed circuit board (PCB) and into the source light guide (shown in Figure 6 below). The lasers are driven by custom-designed pulse shaping circuitry that efficiently generates laser pulses that are less than 150 ps wide. The lasers operate in gain-switched mode, which enables the production of optical pulses that are shorter than the electrical pulse that drives them. The maximum average power from each laser when running at full duty cycle is limited to 5 mW. In operation, due to temporal multiplexing to avoid optical crosstalk between modules, the duty cycle for each laser is ~8%, bringing the average power per source below 1 mW, max.

In addition to the laser driver circuitry and laser diodes, this sub-assembly contains the power conditioning circuits for the module.

2.1.3 Detector Module

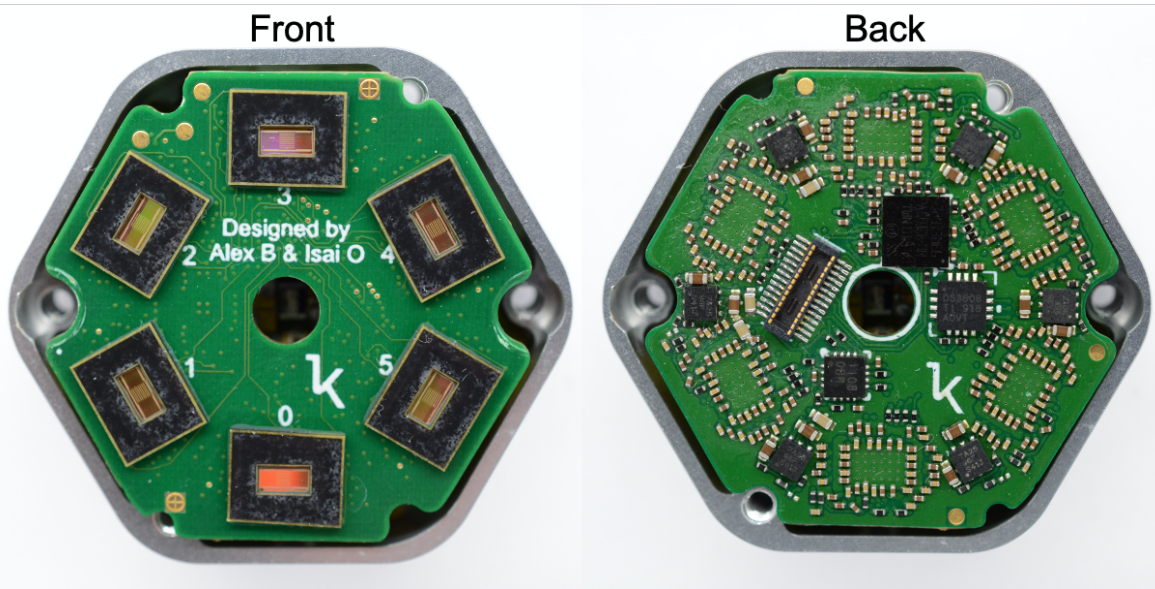


Figure 5. Photos of the detector sub-assembly showing the six Kernel custom detectors (Front) and associated support circuitry (Back).

The detector sub-assembly includes six detector application specific integrated circuits (ASICs) that are custom designed by Kernel and are optimized for performing time-of-flight measurements for diffuse optical tomography. The key time-to-digital conversion (TDC) circuitry is integrated with the photodiodes on each of the ASICs. These custom detectors have been designed for high photon count rates, beyond 1Gcps, without pile-up distortion. Characterization results showing this performance are discussed below.

Photon arrival times from the on-chip TDCs are accumulated into histograms and transmitted over a serial peripheral interface (SPI) bus to a microcontroller. The ASICs in all modules are synchronized to a global 20 MHz reference clock, which allows for recording time-aligned signals from adjacent modules in the system. In addition, each detector ASIC has a dedicated high voltage bias circuitry for optimally biasing each detector.

One detector (labeled 0 in Figure 5) serves as the primary detector within each module. This detector generates the trigger signals to fire the two lasers (690nm and 850nm) within each module.

The integration time for building the histogram on each detector is programmable and ranges from 1ms to 800ms per histogram. For this work, we have configured all sensors to use an integration time of 5ms. Each histogram collected contains signal from only one wavelength. This means our histogram sampling rate is 200 Hz, and, considering both wavelengths, we are able to complete spectroscopic measurements at a rate of 100 Hz.

2.1.4 Module Optics

The optics have been designed to serve multiple objectives – coupling the source laser light from the lasers to the scalp, capturing return light from the scalp, conforming to head curvature, mitigating interference from hair, isolating detected signal between detectors, and maintaining intensity at the detector (Figure 6).

There are a total of 7 light pipes contained within the optical module with 1 source light pipe having a diameter of 3.1mm and 6 detector light pipes each with a 2mm diameter. The source light pipe has a numerical aperture of 0.67

and each of the detector light pipes have a numerical aperture of 0.37. Each of these 7 light pipes are optically isolated from one another to prevent optical cross-talk and signal contamination.

The source light pipe (indicated by a red arrow in Figure 6) is a single rod element that is spring-loaded and hovers over the prism of the laser sub-assembly that is used for combining the two wavelengths of laser light into a single source spot. This light pipe is meant to be tightly coupled to the scalp of the user and light exiting from the tip of the light pipe into air will have a high divergence angle (> 40 degrees), which creates a safe condition should the laser inadvertently be operated when the module is not coupled to the head.

The receiving optics (indicated by the blue arrows in Figure 6) are designed to use springs to comfortably conform the user's head. The input aperture at the end of the detector light pipes is 2mm. We have created a two lens imaging system, consisting of one plano surface, and 3 aspheric surfaces, in order to keep the received optical intensity constant at the detector, regardless of spring compression. The 2mm diameter light pipe that protrudes from the module also helps to comb through hair and prevent blocking the detectors.

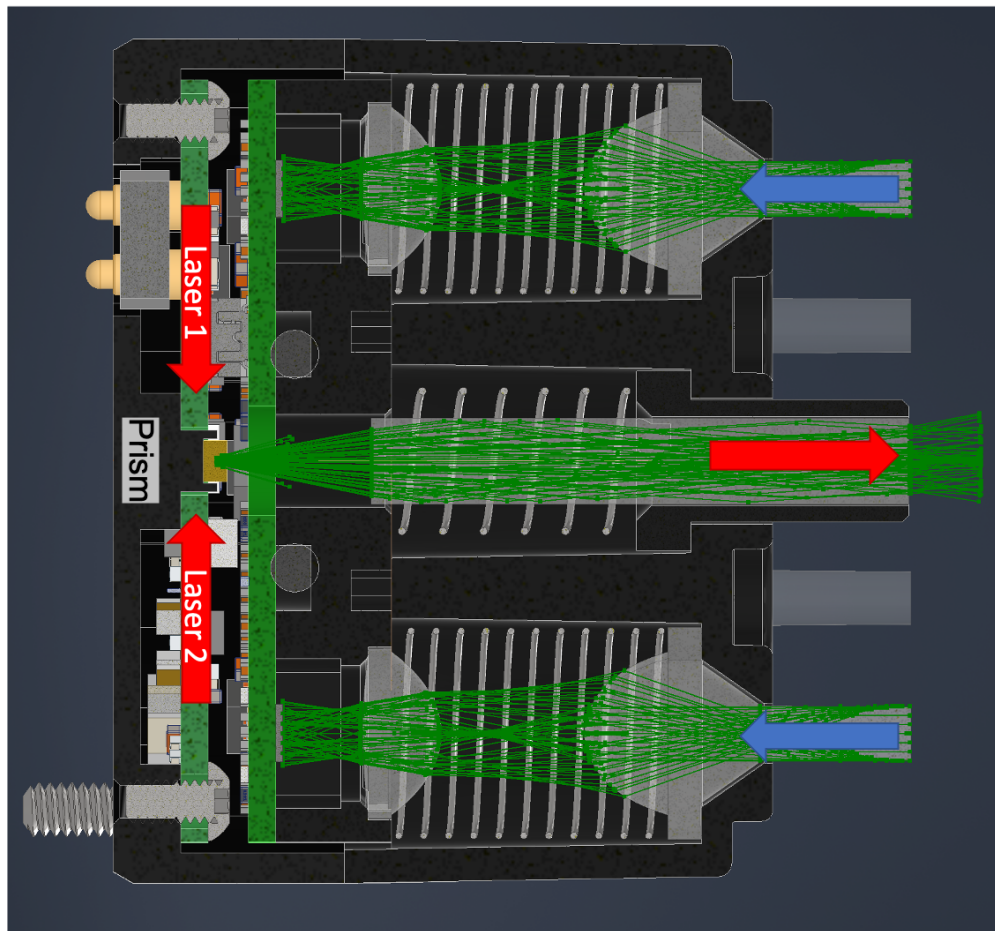


Figure 6. Module cross-section showing the optical configuration of one of the Flow modules. The center light pipe captures the light from the two lasers (690nm and 850nm) after it is reflected off of the prism. The source light leaves the module through a 3.1mm aperture (red arrow). The detector optics are indicated by the blue arrows and are used to image the tip of the detector light pipes onto the custom designed detectors.

2.2 BIP Protocol

The BIP protocol was devised to assess basic hardware performance of time-domain instruments. Here we have characterized detector responsivity, differential non-linearity (DNL), after pulsing, as well as the system's impulse response function (IRF) and its temporal stability.

The detector responsivity assessment in the BIP protocol measures the efficiency of light detection for the time domain system. The responsivity is calculated as the ratio of measured photons exiting from a calibrated phantom vs. the input illumination⁵. For a complete description of the experimental setup, we refer the reader to the original publication⁵. Briefly, the input side of the calibrated phantom was illuminated with a pencil laser beam with power ranging from 0.2 – 2.0 mW and the exiting light was measured with our Gamma module detector, as shown in the schematic in Figure 7.

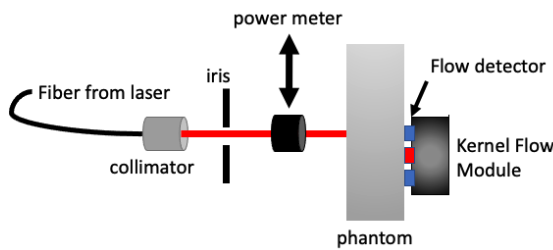


Figure 7. Schematic of setup used for the BIP responsivity measurement.

The DNL measurement in the protocol is to characterize the non-uniformity in the time bin width of the TDCs, which results in a proportionally non-uniform number of photons attributed to each bin. The DNL was measured by applying a uniform illumination source from a battery-powered CW light source for 100 seconds to the detector and measuring the relative differences in the number of collected photons per bin. For our system we found that we got the best correction factor with an illumination at >10^4 counts per bin. The deviation from the ideal equal number of photons bin to bin is calculated as the peak-to-peak difference, normalized by the mean photon counts:

$$\varepsilon_{DNL} = \frac{N_{DNL,max} - N_{DNL,min}}{\bar{N}_{DNL}}. \quad (1)$$

The instrument response function (IRF) measurement is utilized in the BIP protocol to characterize the time resolution of the Kernel Flow system. The IRF is measured with a custom fixture in reflectance mode as shown in Figure 8 as the geometry of the module does not allow for direct source to detector coupling. The source beam is attenuated using a neutral density filter (optical density 0.4) to avoid saturating the detectors with direct illumination and the light is then reflected off a matte surface to redirect it into the collection optics while filling the numerical aperture. The IRF results from a convolution of the laser pulse shape and the temporal response of the detector and associated electronics. Per the protocol, the IRF was measured by averaging 20 histograms of 1s acquisition time.

From the IRF we also calculate the afterpulse ratio, a known signal-dependent source of noise, as defined in the BIP protocol:

$$R_{AP} = \frac{N_{mean,bkg} - N_{mean,dark}}{N_{total,IRF}} \frac{T_{laser}}{\Delta t} \quad (2)$$

Where $N_{mean,bkg}$ and $N_{mean,dark}$ are the average counts of the background measurement in the tail of the IRF and dark count measurements respectively, T_{laser} is the full laser period (1/repetition rate) and Δt is the time bin width. The afterpulsing ratio was calculated for both 690nm and 850nm

Finally, we measured the stability of the IRF to determine the time scale of thermal equilibrium for a single Kernel Flow module. We recorded the stability by taking a continuous measurement starting from a cold start and recording for a period of 1 hour. We analyze the total intensity, the 1st moment, and the shape of the IRF as described in the BIP protocol

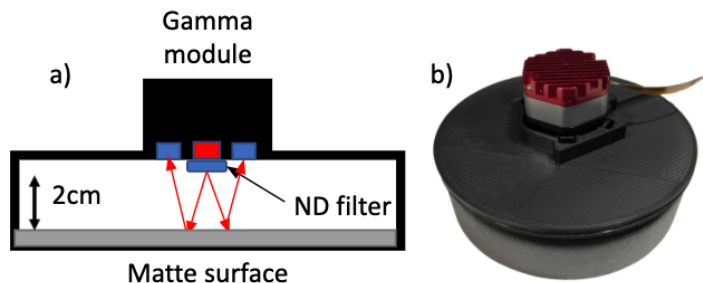


Figure 8. a) Schematic of the custom fixture used to collect an IRF with the Kernel Flow module. b) Picture of the IRF fixture.

2.3 MEDPHOT Protocol: μ_a and μ_s' measurements and fits

The MEDPHOT protocol assesses different photon migration instruments with respect to their ability to recover known optical properties of homogeneous phantoms over a physiologically relevant range⁶. Here we used the Kernel Flow module to measure a subset of the MEDPHOT kit composed of 12 phantoms (BioPixS, Ireland). The phantom cylinders are 50mm in height and 100mm in diameter and consist of solid phantoms containing titanium dioxide (TiO₂) and absorbing toner in varying concentrations. The phantoms are labeled with a letter (A,B,C,D) and number (3,5,7) in which the letter stands for a nominal scatter value and numbers correspond to absorption values as shown in Figure 9 below.

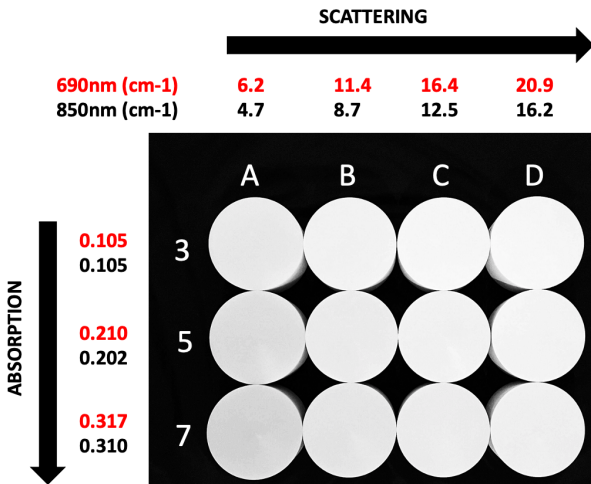


Figure 9. Subset of the MEDPHOT phantoms with their absorption (rows) and scattering (columns) properties. For each row/column, the average value of the absorption/scattering is shown at the two wavelengths at which the Kernel Flow system operates: 690nm (red values) and 850nm (black values) (units are cm⁻¹).

We used a single Flow module to probe the phantoms from the top in a reflectance geometry setup. We estimated the absorption and scattering by minimizing the discrepancy between the measured histogram and a predicted histogram, where the predicted histogram is the result of convolving the measured IRF with an analytical temporal point spread function (TPSF). We used the TPSF equation⁷ derived from an analytical semi-infinite diffusion model using Robin boundary conditions.

2.10 Human measurements

One participant completed two tasks, a breath hold task inducing a small hypercapnic challenge, and a Stroop task. In the breath hold task, the participant's inhalation and exhalation were cued for 5 cycles using an expanding or contracting circle in a block of 30 seconds. After the final cued exhale, the participant was then instructed to hold their breath for 20 seconds while a countdown was on the screen. This series of cued breathing and breath hold was repeated 6 times for a total run duration of 5 minutes. For the Stroop task, the participant was cued with the words "red," "yellow," or "blue" written displayed in red, yellow or blue letters. In congruent condition blocks, the words matched the color of the text. In mixed condition blocks, the words were sometimes in the matching color and sometimes in another color. For all blocks the participant had to respond by pressing a button indicating which color the text was written in. A trial consisted of a word shown for 500 ms followed by a fixation cross lasting 500ms, for a total subject response window of 1000 ms. The inter-trial interval (ITI) was jittered between 500 ms and 1500 ms, with 24 trials per block. After a 10 second rest period at the start of the task, blocks alternated congruent and mixed conditions with a duration of 48-50 seconds for the blocks and 10 seconds for a rest between blocks where the key to color mapping was displayed as a reminder. The run finished with a 20 second rest period. Five blocks of each condition were presented, alternating between the congruent and mixed conditions, for a total run time of approximately 610 seconds. The study was approved by Advarra IRB (Pro00044754) and the participant gave their written informed consent before beginning the study. The arrangement of the modules is shown in Figure 10. For the breath hold task, 10 modules were placed in the sensorimotor plates and four modules were placed in the prefrontal plates. For the Stroop task, 12 modules were placed over the bilateral prefrontal cortices.

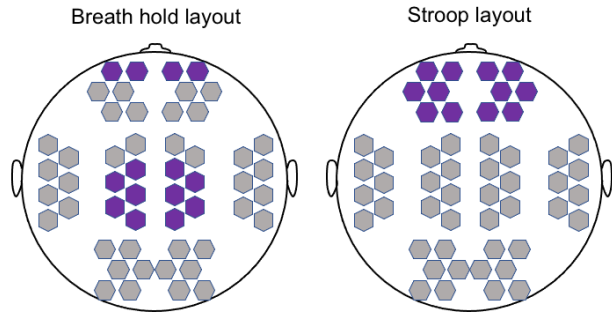


Figure 10. Module layout for human data collection. Left side shows sensorimotor and prefrontal coverage used for the breath hold task, right side shows prefrontal coverage used for the Stroop task.

Data was analyzed using in-house processing software implemented in Python. Processing steps are shown, in order, in Table 1 below. The modified Beer-Lambert Law (mBLL) was used to convert changes in optical density to changes in oxyhemoglobin and deoxyhemoglobin concentrations⁸. Additional standard processing steps were applied as indicated below, and average responses for each block type were calculated.

3. RESULTS AND DISCUSSION

3.1 BIP Protocol

Figure 11 shows the responsivity of the Kernel Flow detector at 690nm and 850nm with different input power ranging from 0.2 - 2.0 mW demonstrating consistent responsivity values over this range. For 690nm, with an input of 2mW we attain a count rate of 1.478 billion counts per second. The DNL deviation in equation (Eq. 1) was calculated as ~0.5, so a DNL correction was applied to the histograms. At 850nm, 2 mW resulted in 0.842 billion counts per second, which is expected due to silicon's lower sensitivity at that wavelength. Throughout this section, all values are for single detectors, of which each Flow module has six.

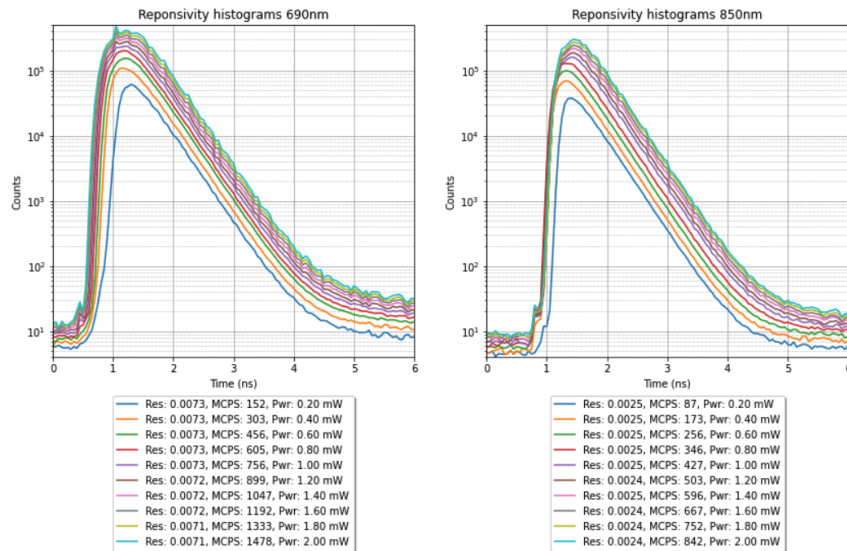


Figure 11. TPSF of laser light transmitted through the BIP phantom for the responsivity measurement at 690 and 850nm.

Table 1. Data processing steps

Step	Parameters
Channel pruning	Removed channels >40mm SDS or with counts below 1e5 per second
DNL correction	Applied using a calibration file collected at the beginning of the session.
Early gate regression	Select a late gate (maximal signal from the brain) and an early gate (minimal signal from the brain) and regress early gate signal from late gate signal after conversion of counts to optical densities.
mBLL	Convert optical density changes to absorption changes (using empirical arrival times instead of a differential path length factor); convert absorption changes to chromophore concentration changes using extinction coefficients ⁹
Motion correction	Temporal derivative distribution repair (TDDR ⁸)
Detrending	Moving average over 100 seconds
Low pass filter	FIR filter with cutoff frequency 0.2Hz (run forward and backward)
Trial averaging	Each trial is baseline corrected using the 5s preceding the event of interest, to remedy potential offsets that are not handled by the detrending step

Figure 12 shows the IRF collected from the Kernel Flow module. The width of the IRF at 50% (FWHM), 10% and 1% are 290, 780, and 1620 ps for 690nm and 350, 1000, and 2150 ps for 850nm. This IRF was measured after thermal stability was attained. The afterpulse ratio, R_{ap} , was calculated to be 0.003 and 0.005 for 690 and 850nm respectively.

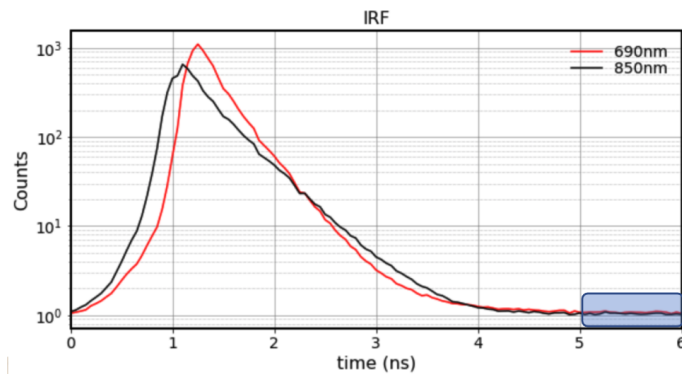


Figure 12. Histogram of the IRF measurement for 690 and 850nm. The boxed region is where the mean background for the afterpulsing ration was selected.

A 1-hr temporal stability measurement of the IRF is shown in Figure 13 displaying the temperature readout from the Flow module, total counts, FWHM, and the mean time of flight (ToF). The temperature is from a calibrated thermistor inside the module. The total counts for 690nm and 850nm lasers are displayed normalized to the 30 min mark and the mean ToF variability is offset to the mean value after warm-up. After the warmup period of 30 mins, we see that the total count shows stability within $\pm 2\%$, FWHM variability for both lasers within ± 10 ps, and the mean ToF variability within ± 10 ps.

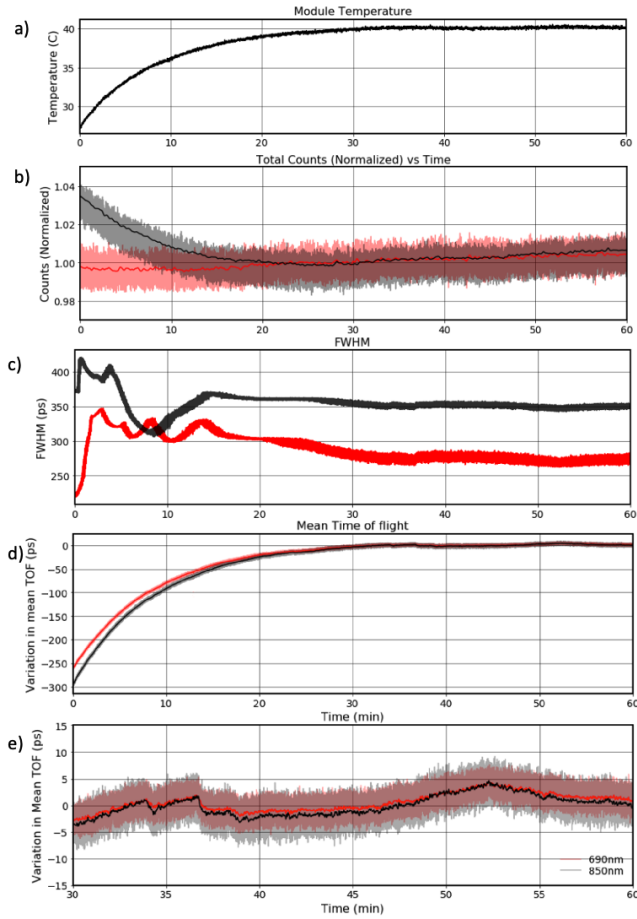


Figure 13. Plots of the 1hr IRF stability measurements showing a) the internal thermistor temperature reading from the Kernel Flow modules b) the total counts of the histogram over time for 690nm (red) and 850nm (black) measurements, c) the FWHM showing the width variation of the histogram over time, d) the change in the mean ToF and e) a close up of the mean ToF from 30-60 mins.

Table 2 shows BIP protocol metrics for the Kernel Flow system and some measurements from other recent high-performance TD-NIRS systems that have reported BIP data. These devices use different source and detector types and vary in size from being wearable to rack-mounted and bench-top systems.

Table 2. Comparison of Kernel Flow with other TD-fNIRS system metrics

	Kernel System			Examples from other TD-NIRS Systems
Detector Responsivity	690nm: 7.2×10^{-9} m ² sr 850nm: 2.5×10^{-9} m ² sr			1×10^{-9} - 4×10^{-7} BIP ⁵ $(3-5) \times 10^{-8}$ Milan Wearable SiPM ¹⁰ 3.3×10^{-8} Milan Probe SiPM ¹¹ 1×10^{-8} - 1×10^{-7} UCL MAESTROS ¹² 3×10^{-9} UCL MONSTIRII ¹²
DNL variation ϵ_{DNL}	<0.5			<0.04 Milan Wearable SiPM ¹⁰ <0.03 Milan Probe SiPM ¹¹ <0.04 Milan 8-wl Rack SiPM ¹³
IRF FWHM	50%	10%	1%	200-270ps Milan Wearable SiPM ¹⁰ 308-556 ps Milan Probe SiPM ¹¹ 10-160ps Milan 8-wl Rack SiPM ¹³ 459 ps UCL MAESTROS ¹² 400-450 ps POLIMI_2 ¹³ 225 ps PTB_4 ^{3,5} 580 ps PTB_2 ^{3,5}
690nm				
290 ps 780 ps 1620 ps				
850nm				
350 ps 1000 ps 2150 ps				
Afterpulse Ratio R _{AP}	690nm: 0.3% 850nm: 0.5%			687nm: 0.21% POLIMI_2 ¹³ 826nm: 0.11%
IRF Stability (after warmup)	N/No variability < $\pm 2\%$ FWHM variability < ± 10 ps Mean TOF variability < ± 10 ps			$\pm 0.5\%$ N/No Milan Probe SiPM ¹¹ ± 10 ps mean TOF $\pm 1\%$ N/No Milan Wearable SiPM ¹⁰ ± 2 ps mean TOF $\pm 1\%$ FWHM over 15 hrs 1 hr stabilize UCL MAESTROS ¹² $\pm 5\%$ N/No < 10 ps mean TOF > 1 hr to stabilize. POLIMI_2 ⁵ $\pm 0.5\%$ N/No ± 5 ps mean TOF < 10 min stabilize. PTB_2 ^{3,5} 0.5% N/No. ± 10 ps mean TOF
Count Rate	> 1500 MCPS			40 MCPS Milan Probe SiPM ¹¹ 1 MCPS Milan Wearable SiPM ¹⁰
Dynamic Range	4-5 orders of magnitude (for 5ms integration time)			2-3 orders of magnitude ^{10-12,14,15}

3.7 MEDPHOT: μ_a and μ'_s measurement and fitting

Plotted in Figure 14 are the nominal values for the 12 phantoms and their estimated values derived from Flow measurements. The nominal values of the phantoms are calibrated with a 2% coefficient of variation but the absolute optical properties are limited by the model uncertainties in the final manufacturer characterization. The model used in this process is based on is described here¹⁶. The measured values consist of approximately 330 individual 5ms histograms for each phantom and wavelength. We used no outlier rejection or other data cleaning. These results include every bin of every histogram from every sensor on the Flow module for each phantom measurement session.

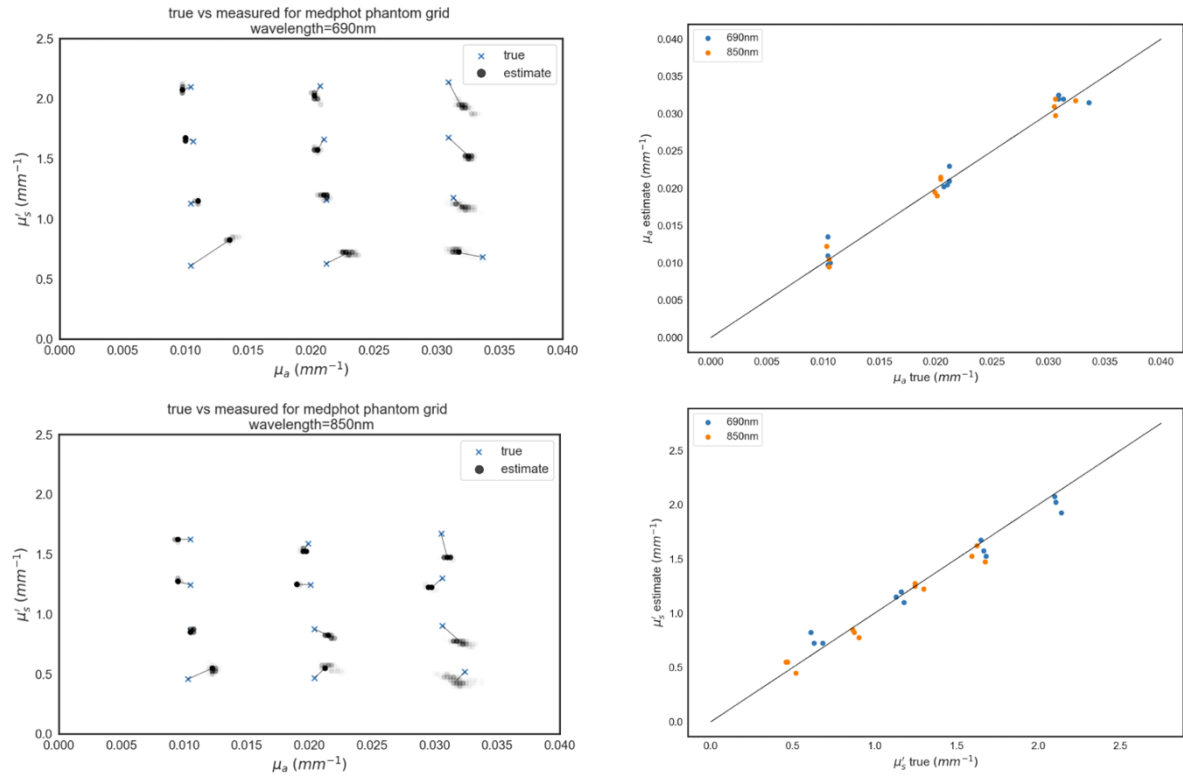


Figure 14. Left column: The nominal μ_a and μ'_s value of the 12 phantoms (blue x's) and the estimated values derived from measurements by the Flow module, at 690 nm. Each 5ms histogram generates an independent measurement, plotted in black but with an opacity of alpha=0.01. Thus, pale gray means few histograms result in estimates at those values while black indicates dozens to hundreds of estimates at that value. Thin black lines connect the nominal value to the median of estimates, to guide the eye. Top panel, 690 nm results, bottom panel, 850 nm. Right column: Top panel: Nominal μ_a vs estimated μ_a . Correlation coefficients are .988 and .993 for 690 nm and 850 nm, respectively. Bottom panel: Nominal μ'_s vs estimated μ'_s . Correlation coefficients are .989 and .984 for 690 nm and 850 nm.

Both the nominal optical properties and our measured values contain hard-to-quantify model uncertainties, for which there is no consensus¹¹. This uncertainty means we cannot evaluate if our measurements are accurate to within phantom property uncertainties. However, as seen in Figure 14 (right column) and Table 3, our optical property estimates are highly correlated with the nominal values, have excellent linearity, and have generally small deviations from the nominal values, averaging to 6.1% for μ_a and 8.2% for μ'_s across wavelengths.

Table 3. Percent deviation of predicted values from nominal values. The nominal values correspond to the 12 phantoms.

Nominal Values (cm^{-1})				Deviation from Nominal (%)			
690 nm		850 nm		690 nm		850 nm	
μ_a	$\mu_{s'}$	μ_a	$\mu_{s'}$	μ_a	$\mu_{s'}$	μ_a	$\mu_{s'}$
0.105	6.2	0.105	4.7	29.8%	35.0%	18.9%	19.8%
0.210	6.2	0.202	4.7	8.5%	15.3%	4.2%	17.2%
0.317	6.2	0.310	4.7	6.3%	6.1%	2.0%	13.3%
0.105	11.4	0.105	8.7	5.8%	1.8%	0.0%	1.9%
0.210	11.4	0.202	8.7	0.9%	3.2%	5.4%	5.8%
0.317	11.4	0.310	8.7	2.2%	6.7%	4.6%	14.4%
0.105	16.4	0.105	12.5	5.7%	1.6%	9.5%	2.4%
0.210	16.4	0.202	12.5	2.4%	5.4%	5.5%	0.2%
0.317	16.4	0.310	12.5	5.2%	9.2%	2.8%	5.8%
0.105	20.9	0.105	16.2	6.3%	1.2%	9.5%	0.1%
0.210	20.9	0.202	16.2	2.2%	3.9%	2.0%	4.2%
0.317	20.9	0.310	16.2	3.6%	10.1%	1.6%	11.9%
Average Deviation				6.6%	8.3%	5.5%	8.1%

3.9 Human measurements

Figure 15 shows an excerpt from a recording from one module on the forehead of a participant. Traces are total counts summed over the histogram. The total counts metric shows an oscillation at a frequency consistent with a heartbeat with a higher magnitude in the 850 nm signal as compared to the 690 nm signal. The ability to measure a heartbeat oscillation with a time domain system is unique and enabled by the 200 Hz sampling rate of our detectors.

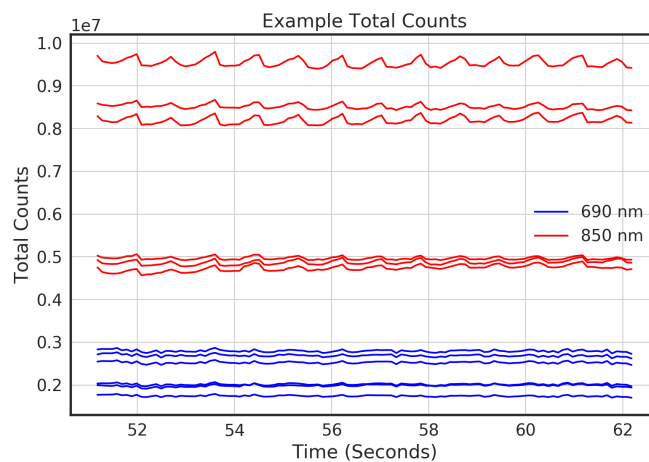


Figure 15. Plot showing total counts for 6 detectors on the forehead of a participant.

An example time course from the breath hold dataset is shown in Figure 16. In this task, consistent with a hypercapnic challenge we see an increase in deoxy hemoglobin shortly after the onset of the breath hold. We can also see oscillations in the oxyhemoglobin trace consistent with the paced breathing in those sections.

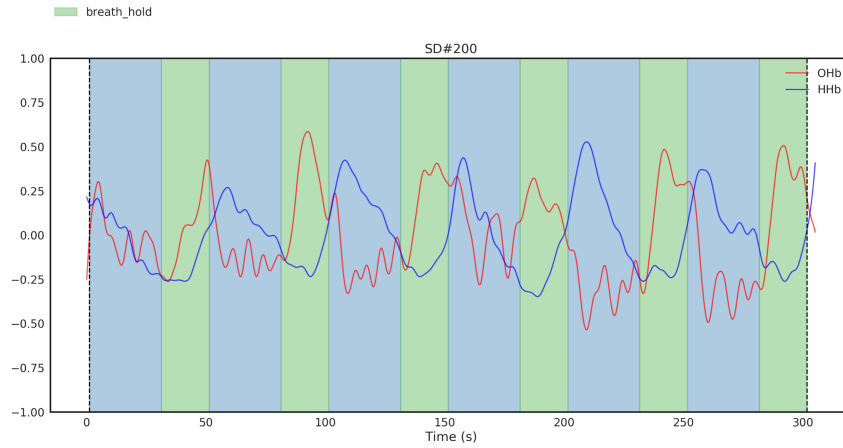


Figure 16. An example time course from the breath hold dataset. Green shading indicates breath hold periods while the blue shading indicates paced breathing.

The block averaged responses for the Stroop task are shown in Figure 17. Channels are averaged over detectors from the same module for clarity. We see a differential response for congruent-only blocks vs. mixed congruent and incongruent blocks. We note larger responses on the more lateral sections of the plot, consistent with activity modulation in the dorsolateral prefrontal cortex.

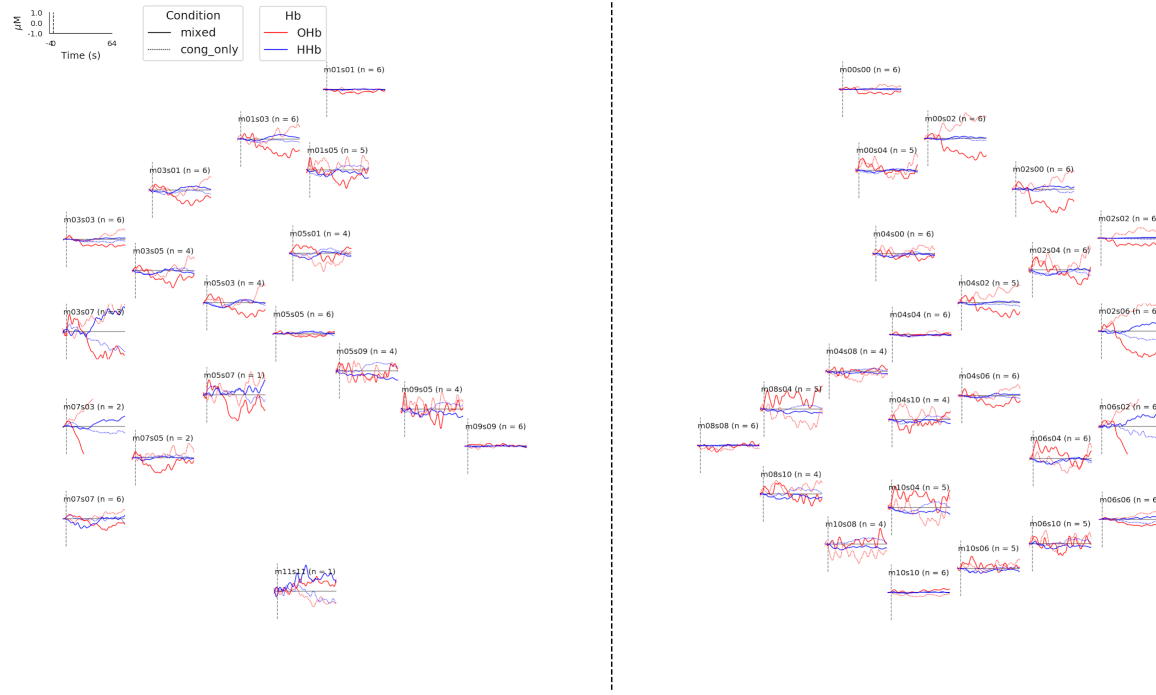


Figure 17. Channel map showing block averages for the Stroop task. Each plot shows an average of detectors as noted (e.g. n=5 indicates an average over 5 usable channels). Red lines show oxyhemoglobin, blue lines are deoxyhemoglobin, dashed lines show the congruent-only condition and solid lines show the mixed congruent and incongruent conditions.

For visualization purposes, we show the response from a single detector in the left lateral portion of the headgear in Figure 18. Here we see that during the congruent-only condition there was an increase in oxyhemoglobin and decrease in deoxyhemoglobin, while the reverse was true during the mixed congruent and incongruent condition.

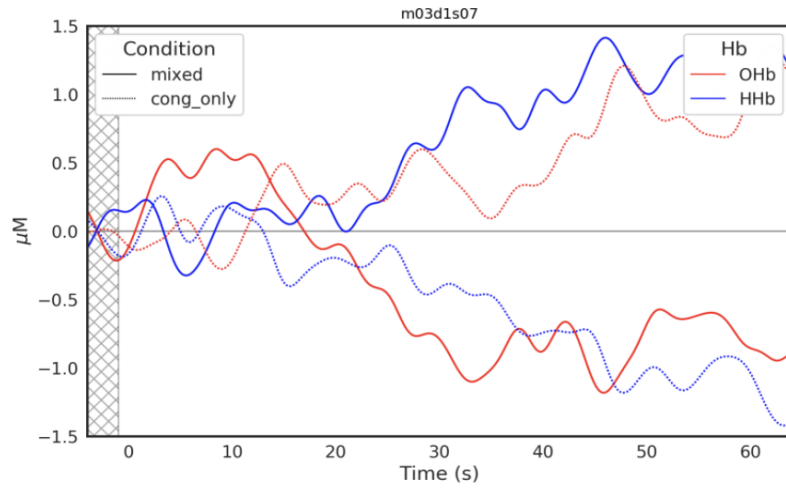


Figure 18. An example averaged response on a single channel. Red lines show oxyhemoglobin, blue lines are deoxyhemoglobin, dashed lines show the congruent-only condition and solid lines show the mixed congruent and incongruent conditions.

4. CONCLUSIONS

In this paper we have described the Kernel Flow system and characterized it using the standard BIP and MEDPHOT protocols. We demonstrate that we have developed a wearable, whole-head coverage TD-fNIRS system that maintains or improves on the performance of existing benchtop TD-fNIRS systems. We additionally show human brain results from a commonly used validation task using Kernel Flow.

ACKNOWLEDGEMENTS

We would like to thank Frédéric Lange and Ilias Tachtsidis for their advice on the measurement protocols, Husam Katnani for his system design guidance, Katriece Ray for her design support, and Bryan Johnson for his product vision and helpful discussions. This work was supported by Kernel.

REFERENCES

- [1] Torricelli, A., Contini, D., Pifferi, A., Caffini, M., Re, R., Zucchelli, L. and Spinelli, L., "Time domain functional NIRS imaging for human brain mapping," *NeuroImage* **85**, 28–50 (2014).
- [2] Wojtkiewicz, S., Gerega, A., Zanoletti, M., Sudakou, A., Contini, D., Liebert, A., Durduran, T. and Dehghani, H., "Self-calibrating time-resolved near infrared spectroscopy," *Biomed. Opt. Express* **10**(5), 2657 (2019).
- [3] Wabnitz, H., Contini, D., Spinelli, L., Torricelli, A. and Liebert, A., "Depth-selective data analysis for time-domain fNIRS: moments vs time windows," *Biomed. Opt. Express* **11**(8), 4224 (2020).
- [4] Lange, F. and Tachtsidis, I., "Clinical Brain Monitoring with Time Domain NIRS: A Review and Future Perspectives," *Applied Sciences* **9**(8), 1612 (2019).
- [5] Wabnitz, H., Taubert, D. R., Mazurenka, M., Steinkellner, O., Jelzow, A., Macdonald, R., Milej, D., Sawosz, P., Kacprzak, M., Liebert, A., Cooper, R., Hebden, J., Pifferi, A., Farina, A., Bargigia, I., Contini, D.,

- Caffini, M., Zucchelli, L., Spinelli, L., et al., "Performance assessment of time-domain optical brain imagers, part 1: basic instrumental performance protocol," *J. Biomed. Opt.* **19**(8), 086010 (2014).
- [6] Pifferi, A., Torricelli, A., Bassi, A., Taroni, P., Cubeddu, R., Wabnitz, H., Grosenick, D., Möller, M., Macdonald, R., Swartling, J., Svensson, T. and Andersson-Engels, S., "Performance assessment of photon migration instruments: the MEDPHOT protocol," *12*.
- [7] Kienle, A. and Patterson, M. S., "Improved solutions of the steady-state and the time-resolved diffusion equations for reflectance from a semi-infinite turbid medium," *J. Opt. Soc. Am. A* **14**(1), 246 (1997).
- [8] Huppert, T. J., Diamond, S. G., Franceschini, M. A. and Boas, D. A., "HomER: a review of time-series analysis methods for near-infrared spectroscopy of the brain," *Appl. Opt.* **48**(10), D280 (2009).
- [9] Prahl, S., "Optical Absorption of Hemoglobin," <http://omlc.ogi.edu/spectra/hemoglobin/index.html>.
- [10] Lacerenza, M., Buttafava, M., Renna, M., Mora, A. D., Spinelli, L., Zappa, F., Pifferi, A., Torricelli, A., Tosi, A. and Contini, D., "Wearable and wireless time-domain near-infrared spectroscopy system for brain and muscle hemodynamic monitoring," *Biomed. Opt. Express* **11**(10), 5934 (2020).
- [11] Di Sieno, L., Behera, A., Rohilla, S., Ferocino, E., Contini, D., Torricelli, A., Krämer, B., Koberling, F., Pifferi, A. and Mora, A. D., "Probe-hosted large area silicon photomultiplier and high-throughput timing electronics for enhanced performance time-domain functional near-infrared spectroscopy," *Biomed. Opt. Express* **11**(11), 6389 (2020).
- [12] Lange, F., Dunne, L., Hale, L. and Tachtsidis, I., "MAESTROS: A Multiwavelength Time-Domain NIRS System to Monitor Changes in Oxygenation and Oxidation State of Cytochrome-C-Oxidase," *IEEE J. Select. Topics Quantum Electron.* **25**(1), 1–12 (2019).
- [13] Re, R., Contini, D., Turola, M., Spinelli, L., Zucchelli, L., Caffini, M., Cubeddu, R. and Torricelli, A., "Multi-channel medical device for time domain functional near infrared spectroscopy based on wavelength space multiplexing," *Biomed. Opt. Express* **4**(10), 2231 (2013).
- [14] Mora, A. D., Martinenghi, E., Contini, D., Tosi, A., Boso, G., Durduran, T., Arridge, S., Martelli, F., Farina, A., Torricelli, A. and Pifferi, A., "Fast silicon photomultiplier improves signal harvesting and reduces complexity in time-domain diffuse optics," *Opt. Express* **23**(11), 13937 (2015).
- [15] Renna, M., Buttafava, M., Behera, A., Zanoletti, M., Sieno, L. D., Mora, A. D., Contini, D. and Tosi, A., "Eight-Wavelength, Dual Detection Channel Instrument for Near-Infrared Time-Resolved Diffuse Optical Spectroscopy," *IEEE J. Select. Topics Quantum Electron.* **25**(1), 1–11 (2019).
- [16] Contini, D., Martelli, F. and Zaccanti, G., "Photon migration through a turbid slab described by a model based on diffusion approximation I Theory," *Appl. Opt.* **36**(19), 4587 (1997).